

# PITTING CORROSION ANALYSIS OF STAINLESS STEEL BY BOUNDARY ELEMENT METHOD WITH STRAIN-DEPENDENT POLARIZATION CURVE

OSAMU KUWAZURU<sup>1</sup>, ARUTO KAWAKAMI<sup>1</sup>, YUMA MIURA<sup>1</sup>, EDUARDO DIVO<sup>2</sup> & ALAIN KASSAB<sup>3</sup>

<sup>1</sup> Department of Nuclear Safety Engineering, University of Fukui, Japan.

<sup>2</sup> Department of Mechanical Engineering, Embry-Riddle Aeronautical University, USA.

<sup>3</sup> Department of Mechanical and Aerospace Engineering, University of Central Florida, USA.

## ABSTRACT

This study aims at evaluating the corrosion rate at the first stage of stress corrosion cracking by a numerical simulation. The stress corrosion cracking starts with a pitting corrosion which appears from a damaged portion of passive film induced by plastic deformation. From micromechanical standpoint, the stress and strain are concentrated around the grain boundaries due to the heterogeneity of microstructures; therefore, the plastic slip occurs mainly around the grain boundaries and generates a fresh surface without passive film. This produces a microcell and affects the macroscopic polarization curve. We obtained this polarization curve of stainless steel from the open-circuit tensile tests associated with the microscopic electrostatic simulations. Moreover, this paper shows the two-dimensional formulation for coupling analysis of elastic stress and electrolytic potential. Both fields are solved by the boundary element method with the discontinuous quadratic element. The strain-dependent polarization curve is used as a nonlinear boundary condition of the potential problem. First, the elastic problem is solved to obtain the surface strain which governs the polarization curve on the surface. Next, the potential problem is solved to obtain the current density on the surface which determines the corrosion rate. Since each node has two corrosion rates in different directions coming from the neighbouring elements, we average these two rates and directions, so as to conserve the volumetric reduction rate unchanged. After moving the nodes as a result of corrosion during the time step, we return to the stress analysis and iterate this procedure during the interested period of time. We demonstrate a corrosion pit growth from a small hemi-elliptic surface defect and show the availability of the proposed method.

**Keywords:** boundary element method, coupling problem, electrochemistry, mechanical damage, oxide film, polarization, stress concentration, stress corrosion.

## 1 INTRODUCTION

With the recent advancement of numerical simulation techniques, corrosion simulations are gathering attention for understanding the insight of localized corosions such as pitting corrosion [1], crevice corrosion [2] and also stress corrosion cracking [3]. Localized corrosion is a highly complicated physical and chemical process consisting of diffusion and migration of ions, convection of fluid, anodic dissolutions and cathodic precipitations. Moreover, the stress-assisted corrosion adds the effect of stress and strain on the anodic dissolution through mechanical damage in the passive film on the material surface. The method most widely used is the finite element method due to its versatility for multi-physics approach and historical advantage in commercial code development [4]. However, the boundary element method (BEM) has also been widely used in corrosion simulation from the early stage of its development [5–8]. While the application of BEM in corrosion simulations is limited to a single physical problem, that is, electrostatics described by Laplace equation, the BEM has two invariable advantages, namely, discretization is easy since the discretization domain is one order of dimension less than the analysis domain and the discontinuity or singularity of field variable can be easily and precisely formulated. Especially, the electric current density must

be discontinuous at the boundary of dissimilar materials, which are in this instance an alloy element grain surrounded by the matrix such as iron or aluminium.

In this study, we focus on the polarization curve of austenitic stainless steel as a boundary condition of the electrostatic field and its dependency on mechanical stress. The polarization curve represents the activity of the anodic and cathodic reactions on the material surface and depends on the surface condition. When applying a mechanical stress, the passive film is microscopically and partially broken due to the stress concentration around the grain boundaries. Then, the bulk material is exposed from the damaged portion of the passive film. The damage of passive film is usually recovered in several tens of minutes by repassivation in an electrolyte solution. However, the impact of mechanical damage on the corrosion is not negligible, since the electrochemical property of the bulk material is completely different from that of the passive film. We have experimentally obtained immediate change in the natural potential of stainless steel during the tensile test in sodium chloride solution. It shows a drastic decrease in natural potential along with plastic elongation. By using this result with the normal polarization curve, the strain-dependent polarization curve is estimated by the microscopic electrostatic analysis by BEM in this study. From the microscopic standpoint, stress and strain must concentrate around the heterogeneity of the microstructure, such as grain boundaries, and moreover, this strain concentration induces the local potential drop through the strain-dependent polarization curve. This is the initiation condition of the localized corrosion assisted by stress. Assuming the existence of stress concentration such as a notch defect, we show the stress–corrosion coupling formulation with a moving boundary modelling based on the BEM. Finally, we show a numerical example concerning a corrosion pit growth from a hemi-elliptic surface defect under a constant stress applied and discuss the availability and validity of the proposed method.

## 2 STRESS–CORROSION COUPLING SIMULATION

### 2.1 Governing equation and boundary conditions

The rigorous governing equation of ion transport in electrolyte solution is the Nernst–Planck equation [4]. In this study, the diffusion and convection are neglected for simplicity and no ion production (chemical reaction) is considered within the solution, except on the material surface. Then, the governing equation can be reduced to a simple potential problem of electrostatic field as Laplace equation

$$\nabla^2 p = 0 \quad (1)$$

where  $p$  is the electrolytic potential. The electroconductivity  $\kappa$  is needed to calculate the current density from the gradient of potential. The boundary condition on the material surface is the polarization curve, that is, the relationship between current density and potential

$$\hat{q} = q(p), \quad (2)$$

where  $\hat{q}$  is the outward normal current density. Note that the potential and current density in the electrostatic analysis are different from the experimentally measured potential  $E$  and current density  $I$  and they hold the relationship [5]

$$p = -E, \quad \hat{q} = -I. \quad (3)$$

As described later, the polarization curve of eqn (2) depends on the mechanical damage in the surface. The dependency on the stress and strain will be introduced in this study.

To evaluate the stress on the material surface, stress analysis is carried out. The linear elastic constitutive equation is adopted for simplicity. The governing equation of elastostatic field without body force is described by the Navier equation

$$\nabla^2 \mathbf{u} + \frac{1}{1-2\nu} \nabla (\nabla \cdot \mathbf{u}) = \mathbf{0} \quad (4)$$

where  $\mathbf{u}$  is the displacement vector and  $\nu$  is Poisson's ratio.

The problem is assumed to be two dimensional. The above two governing eqns (1) and (4) are solved by BEM individually. On the interface between electrostatic and elastostatic fields, however, the surface stress affects the polarization curve, which is the boundary condition of the electrostatic field. In other words, these two problems interact on the interface between them. Moreover, this interface moves as the corrosion develops with anodic dissolution. Since the time scale of this moving boundary is much longer than the ion transportation and stress redistribution, the loose coupling strategy is justifiable and the moving boundary update with a small time step can be conceptually separated from solving the governing equations. Therefore, the simulation procedure is simple: (1) stress analysis with the current interface, (2) potential analysis with the updated polarization curve, (3) update of moving interface with the prescribed time step and repeat (1) through (3) until the end of the prescribed period of simulation time. The electrostatic problem is nonlinear, so the Newton–Raphson method was adopted by considering potential as an independent parameter and current density as a dependent parameter on the interface. The BEM code used in this study was developed by the authors. The discontinuous and three-node curve element was used.

## 2.2 Moving boundary model

The moving velocity of the interface is determined by Faraday's law based on the current density. Assuming that the potential analysis for present time  $t$  was done, the moving velocity normal to the surface of node  $i$  of  $n$ -th element is described by

$${}^t \mathbf{v}_i^n = -\frac{M}{zF\rho} {}^t \hat{q}_i^n {}^t \mathbf{n}_i^n, \quad (5)$$

where  $M$  is the atomic mass,  $z$  the valence of dissolved metal ion,  $\rho$  the mass density,  $F$  the Faraday constant and  ${}^t \mathbf{n}_i^n$  the outward unit normal vector at node  $i$  of  $n$ -th element. Note that now we are using the discontinuous quadratic element which has all the nodes inside it; therefore, the current density has to be extrapolated from the internal nodes for field variables to the geometric node at the end of line element and is used in eqn (5).

The magnitude and direction of the moving velocity is not always continuous at the element boundary (joint of line elements). To keep the moving velocity continuous, we modify the nodal velocity by the sense of averaging. Consider the globally counted  $I$ -th node which connects  $n$ -th element to  $n+1$ -th element. The nodal position of  $n$ -th quadratic element at time  $t$  is denoted by  ${}^t \mathbf{x}_i^n$  ( $i = 1, 2, 3$ ), as shown in Fig. 1. As a nature of element discretization, the moving velocity vectors  ${}^t \mathbf{v}_3^n$  and  ${}^t \mathbf{v}_1^{n+1}$  do not always coincide in their magnitude and direction. The moving direction in this study is fixed to the mid-angle between those two velocity vectors and described by the outward normal vectors as

$${}^t \mathbf{n}_I = \left( {}^t \mathbf{n}_3^n + {}^t \mathbf{n}_1^{n+1} \right) / \left| {}^t \mathbf{n}_3^n + {}^t \mathbf{n}_1^{n+1} \right|. \quad (6)$$

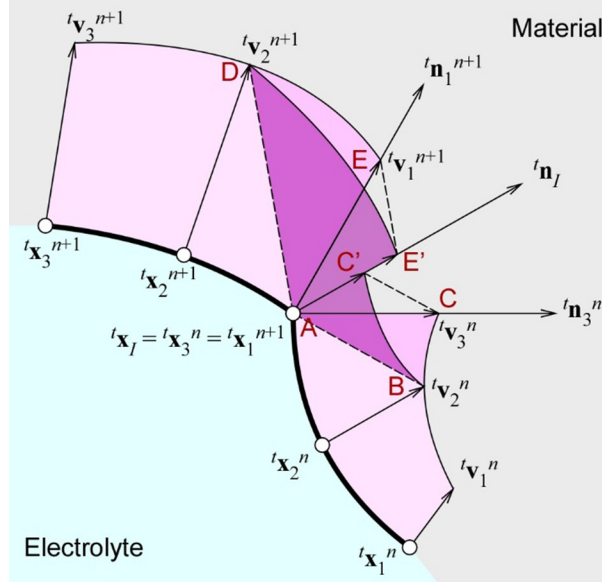


Figure 1: Moving velocity of  $I$ -th node and its correction to conserve the dissolved volume.

Next the moving velocities  $'\mathbf{v}_3^n$  and  $'\mathbf{v}_1^{n+1}$  are projected to the direction  $'\mathbf{n}_I$  so as to conserve the dissolved volume in a unit time (areas of triangles ABC and AED). To keep the areas of triangles ABC and AED, the points C and E move parallel to the lines AB and AD and reach the points C' and E', respectively. Thus, the projecting direction is determined based on the geometrical configuration as

$$'a_3^n = \left( 'x_3^n - 'x_2^n - 'v_2^n \right) / \left| 'x_3^n - 'x_2^n - 'v_2^n \right|, \quad (7)$$

$$'a_1^{n+1} = \left( 'x_1^{n+1} - 'x_2^{n+1} - 'v_2^{n+1} \right) / \left| 'x_1^{n+1} - 'x_2^{n+1} - 'v_2^{n+1} \right|. \quad (8)$$

Denoting the distances of projection as  $\alpha^n$  and  $\alpha^{n+1}$ , the modified nodal velocities are obtained as

$$\tilde{v}^n 'n_I = 'v_3^n + \alpha^n 'a_3^n, \quad (9)$$

$$\tilde{v}^{n+1} 'n_I = 'v_1^{n+1} + \alpha^{n+1} 'a_1^{n+1}. \quad (10)$$

Finally, the velocity of  $I$ -th node is determined by averaging these two velocities as

$$'v_I = \frac{\tilde{v}^n + \tilde{v}^{n+1}}{2} 'n_I. \quad (11)$$

The nodal position is updated with the time step  $\Delta t$  by using the continuous velocity field obtained by eqn (11) as

$${}^{t+\Delta t} \mathbf{x}_3^n = {}^{t+\Delta t} \mathbf{x}_1^{n+1} = {}^{t+\Delta t} \mathbf{x}_I = {}^t \mathbf{x}_I + {}^t \mathbf{v}_I \Delta t. \quad (12)$$

Note that when  $'\mathbf{n}_1^{n+1}$  was opposite to  $'\mathbf{n}_3^n$  as in case of crack, the mid-angle direction  $'\mathbf{n}_I$  is obtained by rotating  $'\mathbf{n}_3^n$  by  $\pi/2$  counterclockwise instead of eqn (6).

### 2.3 Strain-dependent polarization curve

We obtained the polarization curve of 316 stainless steel without stress in aerated 1 mass% NaCl solution of room temperature by the electrochemical experiment. The result is shown by the black solid line in Fig. 2, where the vertical axis means the absolute value of current density. In practice, the cathodic part on the left side of the curve has a negative current. Its anodic part and cathodic part were individually approximated by the empirical equation as

$$I = \left\{ C + \frac{D}{1 + \exp[-(E - E_1)/B]} \right\} (E - E_0), \quad (13)$$

where  $B$ ,  $C$ ,  $D$ ,  $E_0$  and  $E_1$  are the fitting parameters [9]. This curve is used as the polarization curve of intact portion of the material surface. The fitting results are shown by the blue solid line in Fig. 2.

To determine the polarization curve of the damaged portion, we used the relationship between natural potential and applied stress obtained by the fast tensile test in 1 mass% NaCl solution with open-circuit measurement. Figure 3 shows the relationship between true stress and true strain which were calculated from the nominal stress and nominal strain measured by the strain gauge. The strain gauge was broken before reaching the tensile strength. The breaking point was estimated by using the minimum cross-sectional area measured after the tensile test. The unknown part from the gauge failure to the specimen failure was linearly interpolated as shown in Fig. 3. To determine the stress corresponding to an arbitrary strain uniquely, this relationship was approximated by the empirical equation as

$$\sigma = 1280 \varepsilon^{0.3185}. \quad (14)$$

The above equation will be used to convert the stress-dependent polarization curve to the strain-dependent one, as shown subsequently.

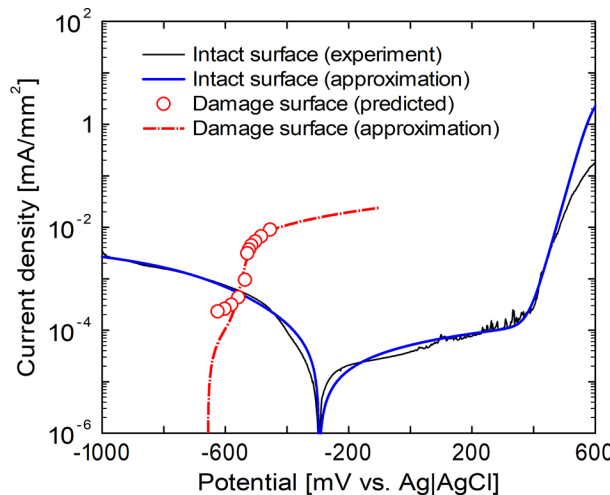


Figure 2: Polarization curves for intact and damaged portions.

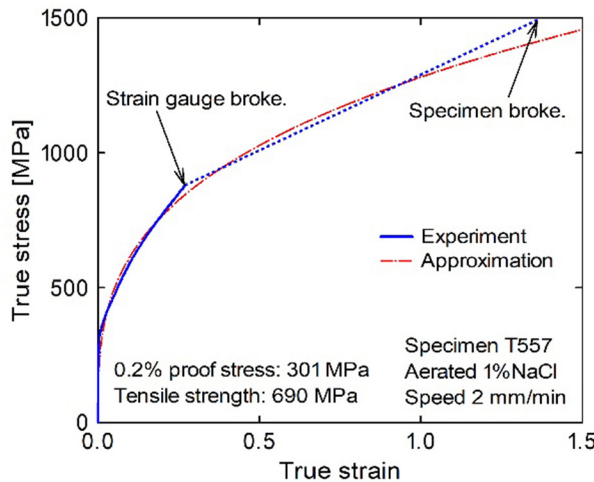


Figure 3: Relationship between true stress and true strain.

Figure 4 shows the relationship between natural potential and true stress which was measured during the tensile test. Since the strain rate is reasonably fast, almost no effect of repassivation is included in this result. This potential decrease due to stress was used to determine the polarization curve of the damaged portion. When applying the stress over the yield stress, a lot of damaged surface without passive film is generated by the plastic strain. Then, many microcells are constituted and the micro-current flows from damaged portions to intact portions keeping the self-equilibrium, which means that the average current density is null. In this condition, the potential distribution is almost uniform [9]. Hence, by assuming the uniform potential and null average current density, the potential and local current density on the damaged portions can be calculated as follows. The plastic strain  $\varepsilon_p$  is determined by the applied stress based on the experimental data in Fig. 3.

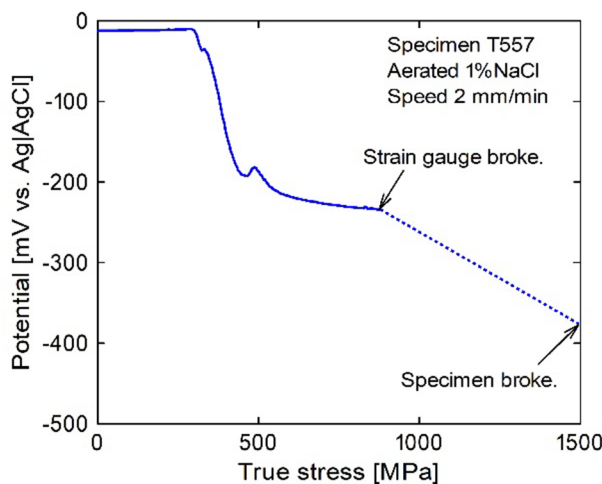


Figure 4: Relationship between open-circuit potential and true stress.

$$\varepsilon_p = \varepsilon - \frac{\sigma}{E}, \quad (15)$$

where  $E$  is the Young's modulus. In the above equation, the strain is defined in logarithmic sense. Therefore, the plastic strain was converted to nominal one. This nominal plastic strain  $\varepsilon_{np}$  is regarded as the ratio of the damaged portion to the intact portion (damage ratio). On the other hand, the potential drop by the applied stress is determined by the experimental data in Fig. 4. The natural potential decreases by this drop from the intact state ( $-296$  mV), and the decreased potential  $E_{int}$  prescribes the local cathodic current density  $I_{int}$  on the intact portions by the cathodic polarization curve of the intact surface using eqn (13). Then, the local anodic current  $I_{dam}$  on damaged portions has to be equal to the local cathodic current due to the assumption of null average current density. Thus, the local anodic current density  $I_{dam}$  corresponding to the applied stress can be calculated according to the damage ratio as

$$I_{dam} = -\frac{I_{int}}{\varepsilon_{np}}. \quad (16)$$

The potential of damaged portions  $E_{dam}$  is almost the same as  $E_{int}$  [9]. Thus, several sets of  $E_{dam}$  and  $I_{dam}$  corresponding to selected stress values were calculated and plotted as red open circles in Fig. 2. Moreover, these plots were approximated by using the empirical formula in eqn (13) again. This curve is the identified polarization curve of the damaged portion. The cathodic polarization curve of the damaged portion was assumed to be parallel to that of the intact portion. The obtained results of the fitting parameters are listed in Table 1.

To obtain the stress-dependent polarization curve, the microcell of a single damaged portion located at the centre of passive film as shown in Fig. 5 was evaluated by BEM. The number and size of microcells does not affect the average potential and average current density [9]; therefore, this single unit cell analysis is justified. The intact portion of the passive film and the damaged portion have the polarization curves obtained in eqn (13) and Table 1, respectively. The width and height were fixed to  $L = 1$  mm and  $H = 10$  mm, respectively. The damage ratio  $r/L$  was determined by the nominal plastic strain corresponding to the prescribed stress. To obtain the polarization curve, some current density corresponding to the experimental current density is applied on the top of electrolyte. Then, the distributions of potential and current density on the material surface were calculated by BEM and the average potential on the material surface was evaluated. By changing the applied current density, the polarization curve at that stress was obtained. Some example results are shown in Fig. 6. Note that these polarization curves are the electrochemical property immediately after the loading, since the potential recovery by repassivation was not considered.

Table 1: Parameters of polarization curves of intact and damaged portions.

	Intact portion		Damaged portion	
	Anodic	Cathodic	Anodic	Cathodic
$B$ (mV)	31.2	-150	13.1	-150
$C$ (S/mm <sup>2</sup> )	$1.25 \times 10^{-7}$	$5.52 \times 10^{-7}$	$1.73 \times 10^{-6}$	$5.52 \times 10^{-7}$
$D$ (S/mm <sup>2</sup> )	$2.95 \times 10^{-4}$	$3.47 \times 10^{-6}$	$4.12 \times 10^{-5}$	$3.47 \times 10^{-6}$
$E_1$ (mV)	576.6	-600	-526.6	-960.5
$E_0$ (mV)	-296.3	-296.3	-656.8	-656.8

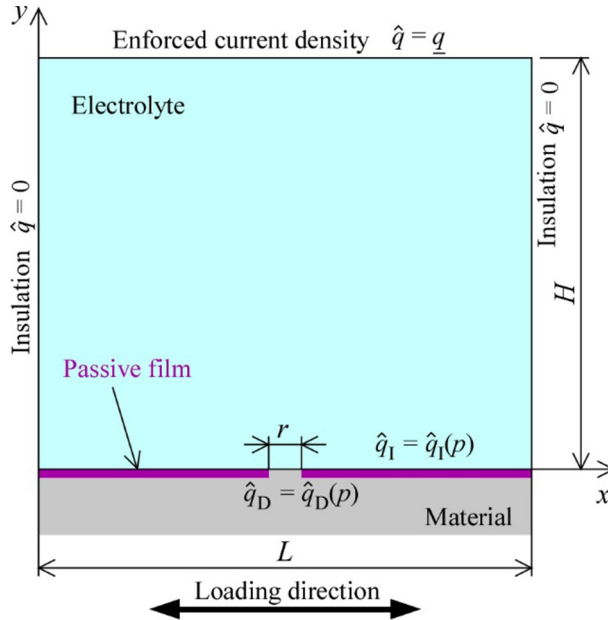


Figure 5: Damaged passive film model to determine the polarization curve.

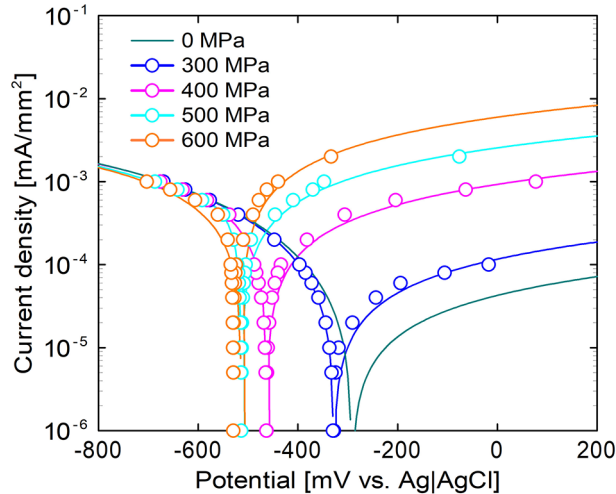


Figure 6: Polarization curves in stressed state without repassivation calculated by BEM.

The fitting parameters in the polarization curve of eqn (13) were determined by fitting to the simulation results at each stress level and their dependency on the stress was examined. As a result, we obtained the stress-dependent fitting parameters as

$$X = X_0 + \frac{\Delta X}{1 + \exp[-(\sigma - \sigma_0)/\sigma_w]}, \quad (17)$$

Table 2: Stress dependency parameters for anodic polarization curve.

$X$	$X_0$	$\Delta X$	$\sigma_0$	$\sigma_w$
$B$ (mV)	1.95	67.6	486	73.3
$C$ (S/mm <sup>2</sup> )	$1.46 \times 10^{-7}$	$2.71 \times 10^{-5}$	626	82.9
$D$ (S/mm <sup>2</sup> )	$6.91 \times 10^{-5}$	$1.04 \times 10^{-3}$	566	74.3
$E_1$ (mV)	103	0	0	1
$E_0$ (mV)	-293	-231	361	39

Table 3: Stress dependency parameters for cathodic polarization curve.

$X$	$X_0$	$\Delta X$	$\sigma_0$	$\sigma_w$
$B$ (mV)	1.26	239	412	-41.4
$C$ (S/mm <sup>2</sup> )	$4.47 \times 10^{-6}$	$8.27 \times 10^{-7}$	393	37.4
$D$ (S/mm <sup>2</sup> )	$-5.50 \times 10^{-6}$	$3.15 \times 10^{-5}$	449	32.1
$E_1$ (mV)	-500	0	0	1
$E_0$ (mV)	-293	-231	361	39

where  $X$  denotes one of  $B$ ,  $C$ ,  $D$ ,  $E_0$  and  $E_1$ , collectively, and  $X_0$ ,  $\Delta X$ ,  $\sigma_0$  and  $\sigma_w$  are the fitting parameters. As a result of fitting to the relationship between the parameters and stress, we found the parameters as listed in Tables 2 and 3.

Although the obtained polarization is stress dependent as mentioned above, the stress can be easily converted to strain by using eqn (14). The numerical example presented subsequently demonstrates the corrosion analysis coupled with the linear elastic analysis, where the plastic deformation is not considered. Since the stress is overestimated in the elastic analysis, the mechanical damage should be evaluated based on the strain. Then, the strain-dependent polarization curve obtained by combining eqns (13), (14) and (17) with Tables 2 and 3 can be used.

### 3 NUMERICAL EXAMPLE

Here, an example of the corrosion–stress coupling simulation is shown. A small hemi-elliptic surface defect was considered, as shown in Fig. 7. The stress concentration factor is 2.38. The solid material is 316 stainless steel, and the electrolyte is 1 mass% NaCl solution at room temperature. Young's modulus is 212 GPa, Poisson's ratio is 0.3, and the electroconductivity of the electrolyte is 1.76 S/m. The atomic parameters were averaged by considering all of the main alloy elements and determined as  $z = 2.17$ ,  $\rho = 7.864$  g/cm<sup>3</sup>,  $M = 55.47$  g/mol. A nominal tensile stress of 150 MPa is applied and held parallel to the surface. The surface stress is calculated by Cauchy's formula based on the normal vector and stress tensor at the node, and the polarization is determined from this surface stress by using eqns (13) and (17). In other words, the stress-dependent polarization curve was used as the first trial calculation. The time step was fixed to 2 h. The repassivation of damaged passive film and precipitation of corrosion products were completely neglected. The discontinuous and quadratic curve element was used for discretization and the total number of elements was 360.

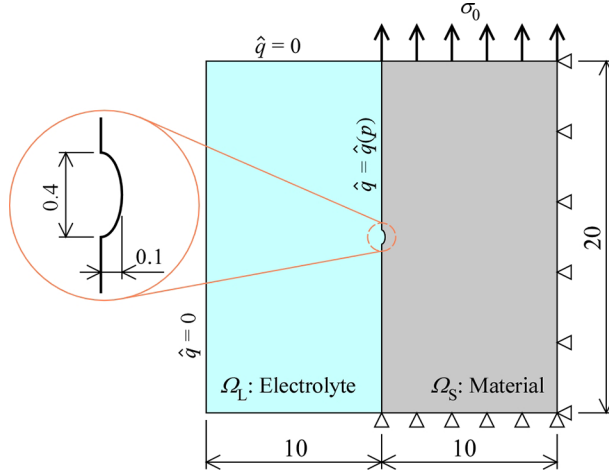


Figure 7: Stress–corrosion coupled model with a small surface defect (unit: mm).

The result of moving interface is depicted in Fig. 8, where the notch root is magnified. Until around the point of 100 h, the corrosion developed almost uniformly and after it, the corrosion suddenly concentrated to the centre of notch root. The shape is gradually sharpened and after the point of 120 h at which the shape reached a completely sharp V-notch, the calculation diverged. At this point in time, the stress at the edge of V-notch will be infinity similar to the crack tip and this stress singularity leads to unstable development of the edge of notch. Therefore, we need to modify the moving boundary method, so as to consider the refinement of mesh, inclusion of stress singularity and stabilization of corrosion development in our future works. The above result shows that the surface defect of stress concentration factor of 2.38 is locally corroded and initiates a stress corrosion crack around 120 h after the corrosion begins if the repassivation never happened. The stress-dependent polarization curve

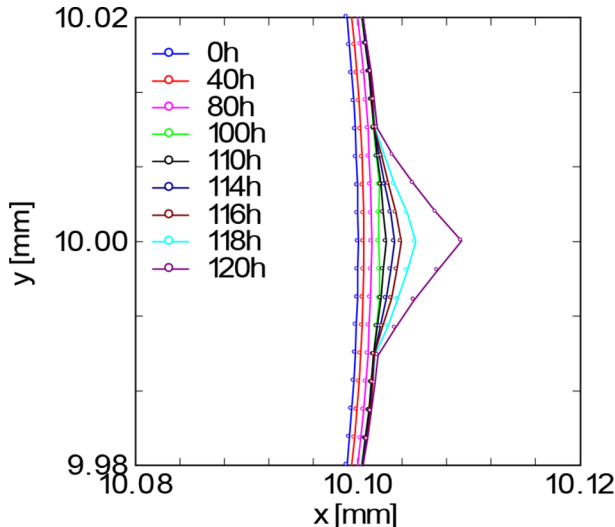


Figure 8: Development of pitting corrosion evaluated by the coupling analysis.

also accelerated the corrosion development. Of course, this is not true and the repassivation definitely happens. Hence, we have to further introduce a repassivation model in the strain-dependent polarization curve.

#### 4 CONCLUSION

A method of stress–corrosion coupling simulation was proposed and a BEM code was developed. Based on the results of the open-circuit tensile test, the normal polarization test without stress and the BEM simulation with the damaged passive film model, we found the stress- and strain-dependent polarization curve of austenitic stainless steel. Using this curve, the interaction between stress and corrosion was formulated and the moving boundary method to predict the development of corrosion front was proposed. The numerical example using the small surface defect model demonstrates the availability of the proposed formulations and the possibility to predict the transition from the pitting corrosion to crack. At the same time, the numerical instability of the moving boundary was confirmed.

#### ACKNOWLEDGEMENTS

This study was financially supported by Japan Society for the Promotion of Science (JSPS) KAKENHI 15KK0233. The authors thank Mr. Koichi Hira (University of Fukui) for his technical assistance in the experiments.

#### REFERENCES

- [1] Brewick, P.T., Kota, N., Lewis, A.C., DeGiorgi, V.G., Geltmacher, A.B. & Qidwai, S.M., Microstructure-sensitive modelling of pitting corrosion: Effect of the crystallographic orientation. *Corrosion Science*, **129**, pp. 54–69, 2017. <https://doi.org/10.1016/j.corsci.2017.09.009>
- [2] Sun, W., Wang, L., Wu, T. & Liu, G., An arbitrary Lagrangian-Eulerian model for modelling the time-dependent evolution of crevice corrosion. *Corrosion Science*, **78**, pp. 233–243, 2014. <https://doi.org/10.1016/j.corsci.2013.10.003>
- [3] Nguyen, T.T., Bolivar, J., Shi, Y., Réthoré, J., King, A., Fregonese, M., Adrien, J., Buffiere, J.Y. & Baietto, M.C., A phase field method for modelling anodic dissolution induced stress corrosion crack propagation. *Corrosion Science*, **132**, pp. 146–160, 2018. <https://doi.org/10.1016/j.corsci.2017.12.027>
- [4] Liu, C. & Kelly, R.G., A review of the application of finite element method (FEM) to localized corrosion modelling. *Corrosion*, **75(11)**, pp. 1285–1299, 2019. <https://doi.org/10.5006/3282>
- [5] Aoki, S. & Kishimoto, K., Prediction of galvanic corrosion rates by the boundary element method. *Mathematical and Computer Modelling*, **15(3–5)**, pp. 11–22, 1991. [https://doi.org/10.1016/0895-7177\(91\)90049-d](https://doi.org/10.1016/0895-7177(91)90049-d)
- [6] Aoki, S. & Amaya, K., Optimization of cathodic protection system by BEM. *Engineering Analysis with Boundary Elements*, **19**, pp. 147–156, 1997. [https://doi.org/10.1016/s0955-7997\(97\)00019-2](https://doi.org/10.1016/s0955-7997(97)00019-2)
- [7] Butler, B.M., Kassab, A.J., Chopra, M.B. & Chaitanya, V., Boundary element model of electrochemical dissolution with geometric non-linearities. *Engineering Analysis with Boundary Elements*, **34**, pp. 714–720, 2010. <https://doi.org/10.1016/j.enganabound.2010.03.007>
- [8] Lan, Z., Wang, X., Hou, B., Wang, Z., Song, J. & Chen, S., Simulation of sacrificial anode protection for steel platform using boundary element method. *Engineering Anal-*

- ysis with Boundary Elements, **36**, pp. 903–906, 2012. <https://doi.org/10.1016/j.enganabound.2011.07.018>
- [9] Kuwazuru, O., Ode, K., Yamada, M., Kassab, A.J. & Divo, E., Experimental and boundary element method study on the effect on polarization curve of cast aluminum alloy in sodium chloride solution. *Corrosion Science*, **132**, pp. 136–145, 2018. <https://doi.org/10.1016/j.corsci.2017.12.019>